Cholesterol-mediated activation of VapC12 toxin modulates growth and drug susceptibility in *Mycobacterium tuberculosis*

Zohra Hashmi[1], Shivendra Pratap Singh[3#], Sakshi Talwar[1#], Abhin Kumar Megta[3], Mitul Srivastava[2], Debapriyo Sarmadhikari[2], Taruna Sharma[1], Chandresh Sharma[1] Shailendra Asthana[2*], Vengadesan Krishnan[3*], Amit Kumar Pandey[1*]

[1]Mycobacterial Pathogenesis Laboratory, Centre for Tuberculosis Research, BRIC-Translational Health Science and Technology Institute, Haryana, India

[2]Computational Biophysics and CADD Group, Computational and Mathematical Biology Centre (CMBC), BRIC-Translational Health Science and Technology Institute, Faridabad, Haryana, India

[3]Lab of Structural Microbiology, Regional Centre of Biology, Faridabad, Haryana, India

 # Contributed equally to the work

***Correspondence**

Shailendra Asthana: sasthana@thsti.res.in

Krishnan Vengadesan: kvengadesan@rcb.res.in

Amit Kumar Pandey: amitpandey@thsti.res.in

Abstract

Tuberculosis eradication efforts are severely hampered by antimicrobial resistance (AMR). We have previously reported that VapBC12 TA system in *Mycobacterium tuberculosis* (*M. tuberculosis*) regulates both disease and antibiotic persistence in tuberculosis. In this study, we developed a mechanistic understanding of the VapBC12-dependent modulation of growth and antibiotic susceptibility in *M. tuberculosis*. We identified a unique **C**holesterol **R**ecognition **A**mino acid **C**onsensus

(CRAC) motif in VapC12 toxin and demonstrated that its heterologous expression induces toxicity in *M. smegmatis*. We have solved the crystal structure of VapB12 antitoxin at a 1.6A^0 wavelength and using molecular modeling predicted the structure of TA complex. Structure-function analysis revealed specific residues critical for the assembly and activity of the VapBC12 TA system. Our study suggests that cholesterol activates the VapC12 toxin by competitively displacing its cognate antitoxin at the CRAC motif which consequently restricts the growth of *M. tuberculosis*. Finally, we demonstrated that chemical inhibition of VapC12 prevents growth restriction and potentiates activity of anti-TB drugs.

Keywords: *M tuberculosis*, TA Complex, VapBC12, Cholesterol, persistence, tolerance, Shortened treatment

Introduction

A steady rise in the frequency of MDR and XDR tuberculosis continuously challenges global tuberculosis eradication deadlines[1]. The ability of *M. tuberculosis* to persist inside the host and its obstinate tolerance to anti-TB drugs pose a significant challenge in the pursuit of finding a potent anti-TB therapy[2–4]. Thus, targeting such a population is key to finding permanent solutions to the rising threat of antimicrobial resistance in tuberculosis[3–5]. The diverse microenvironments within granulomas create a high degree of heterogeneity permissive for varying bacterial growth, thus generating drug-tolerant persisters[6–8]. The generation of the persister in *M. tuberculosis* has been reported to be regulated by different signaling pathways, including various transcription factors and TA systems. These pathways are known to function as metabolic regulators of growth under different stress conditions such as nutrient deprivation, acidic environment and immune modulations[9–14].

M. tuberculosis possesses a large repertoire of approximately 93 toxin-antitoxin (TA) modules, classified into five families[15]. Among these, the type II VapBC modules have been the most studied TA family. The VapC toxin typically exhibits RNase activity, modulating growth of *M. tuberculosis* by targeting RNA[16–18]. Albeit *M. tuberculosis* contains around 50 VapBC modules, only a few have been structurally and biochemically characterized[19–27], and their role in mycobacterial pathogenesis remains obscure[13,25]. We have previously demonstrated that utilization of host cholesterol is critical for the survival of *M. tuberculosis* during the chronic stage of infection in mice[28]. Subsequently, we showed that VapC12 toxin is essential for the generation of cholesterol-induced persisters in tuberculosis[29]. Interestingly, strain lacking the *VapC12* gene exhibited hypergrowth phenotype in both guinea pig and murine infection models leading to an efficient clearance on antibiotic exposure compared to the wild type strain[30]. This observation aligns with the principle that fast-growing bacteria are more susceptible to anti-TB drugs[31,32].

To get a mechanistic insight, we developed a surrogate *M. smegmatis (M. smegmatis)* -based model system to understand the binding dynamics of the VapBC12 TA system and its implications on the regulation of growth in *M. tuberculosis*. We identified a CRAC motif unique to the VapC12 toxin and demonstrated that it overlaps with the antitoxin binding site. We successfully solved the crystal structure of the VapB12 antitoxin and, by homology modeling predicted that the VapBC12 complex exists in a hetero-octameric form in a “drone” like structure. We further identified residues from both toxin and antitoxin that were critical for the stability and/or the activity of the TA system. Substitution of critical residues present in the CRAC motif of the toxin disrupted the TA binding resulting in the generation of constitutively active toxin dimers. Our data suggests that

cholesterol activates the VapC12 toxin by competitively displacing the VapB12 anti-toxin from the CRAC motif. Interestingly, we found that the binding of both the anti-toxin and the cholesterol to the toxin involves different residues and that an 11-mer peptide, identified from the interacting interface of TA using computational methods to mimic antitoxin, was sufficient to neutralize the activity of the VapC12 toxin. The peptide-mediated inactivation of toxin enhanced the growth of *M. tuberculosis* and potentiated the activity of the anti-TB drugs. The information thus generated in the current study will help to enhance the efficacy of the existing anti-TB regimen by designing novel strategies targeting the generation of persisters during tuberculosis.

Results

VapC12 toxin modulates growth in M. tuberculosis

We began by validating our earlier findings that cholesterol utilisation modulates the growth of *M. tuberculosis*. For this, we introduced a “replication clock” plasmid, pBP10 [33], that, in absence of a selectable marker, is lost at a steady and quantifiable rate. The plasmid was electroporated into both the H37Rv and an isogenic strain deficient in the *vapC12* gene (Δ*vapC12)*(Figure 1a). We first assessed the growth of the WT strain in minimal media supplemented with 0.1% glycerol and 150µM cholesterol. Bacterial counts were enumerated at different time points for both total and plasmid-containing bacteria. As expected, we observed an increase in the plasmid retention time in cholesterol relative to glycerol media, suggesting a reduced growth rate in cholesterol media (Figure 1b). To further confirm the role of VapC12 toxin in imparting the above phenotype, we compare the growth rate between WT and Δ*vapC12* strains on cholesterol using the above protocol. The lack of VapC12 toxin in *M. tuberculosis* led to a significant loss of the clock plasmid, indicating an increased growth rate compared to the WT on cholesterol. Consistent with the

replication clock data, the bacterial density of the Δ*vapC12* increased 10-fold from day 4 to 8 and 5-fold from day 8 to 12, while that of the WT remained relatively constant (Figure 1c). As a control, we did not observe any statistical difference between the bacterial density and plasmid retention time between the WT and *ΔvapC12* strains cultured on glycerol media (Figure S1a). These data confirm our earlier findings that the growth modulation by cholesterol is dependent on the presence of VapC12. To further uncover the link between cholesterol and VapC12 toxin, we developed a surrogate model using *M. smegmatis.* Non-pathogenic nature, less generation time, and the absence of the VapBC12 TA locus in its genome made *M. smegmatis* an ideal organism for the current study. Briefly, VapC12 toxin alone or in combination with VapB12 anti-toxin were expressed in *M. smegmatis* strain expressing luminescence protein (Figure 1d). Overexpression of VapC12 toxin restricted the growth of *M. smegmatis* while co-expression of cognate anti-toxin VapB12 restored the growth of the strain to the level of *M. smegmatis* harbouring the vector alone in both glycerol and cholesterol media (Figure 1e). The same was further validated using spot titre on 7H11 agar plates (Figure 1f), and the standard CFU plating experiments (Figure 1Sb-c). A similar phenotype was observed on 7H9 enriched media (Figure S1d-f). Overall, a relatively pronounced growth restriction phenotype of the VapC12-overexpressing M. smegmatis strain on cholesterol suggests that cholesterol plays a key role as a modulator of VapC12 toxin activity in *M. tuberculosis* (Figure 1f and S1c).

Crystal Structure of VapB12 Antitoxin reveals a unique Zn^{2+} binding domain

Our crystallization attempts with VapBC12 from *M. tuberculosis* produced plate-like crystals in a solution containing 0.2 M ammonium chloride-NaOH pH 6.3 and 20% (w/v) PEG 3350 (Figure S1). These crystals diffracted to a resolution of 1.6 Å and

belonged to the tetragonal space group $P4_1$ (Table 1). Because our attempts to solve the structure by molecular replacement with known toxins and antitoxins as search templates were unsuccessful, we attempted to use the intrinsic anomalous signal observed during data processing. Ultimately, the phase calculation by Zn-SAD (zinc single-wavelength anomalous diffraction) yielded interpretable electron density (Table 1). Residues of the N-terminal region (residues 1–44) of VapB12 were clearly visible in the electron density map, whereas its C-terminal region (residues 45–75) and VapC12 were missing. Despite concerted efforts to co-crystallize the VapBC12 complex, only the density corresponding to the N-terminal region of the VapB12 antitoxin was discernible. The crystal structure revealed the DNA-binding domain of VapB12. Four VapB12 molecules (chains A, B, C, and D) in the asymmetric unit form two homodimers (Figure 2a). The two monomers in the dimer interact with each other with a buried interface surface area of ~1508 $Å^2$, mediated by 30 residues through multiple hydrogen bonds and a strong salt bridge between Glu43 and Arg46. The interface between the monomers in the dimer had a complex formation significant score (CSS) value of 1 in the interface analysis by PISA[34], implying that the interface plays an essential role in complex formation, that is, the functional DNA-binding domain of VapB12. Each monomer displays a typical ribbon-helix-helix (RHH) fold, the common DNA-binding structural motif of antitoxins, with a β1-α1-α2 topology. The β1-strand (residues 2-11) from each monomer forms an antiparallel β-sheet to establish a dimer through multiple interactions, including two strong hydrogen bonds from the main chain of Ala3-Val10 and Ile7-Val5. This β-sheet is flanked by helices α1 (residues 12-24) and α2 (residues 28-43). Helix α2 further stabilizes the dimer through a strong salt bridge between the side chains of Arg36 and Glu43. Moreover, the side chain of Ser30 from helix α2 participates in a

hydrogen bond with the main chain of Arg8 from the β1-strand. The basic residue Arg8 likely interacts with DNA, and its presence in the β1-strand classifies the RHH fold in VapB12 as Type II. Similarly, another hydrogen bond interaction between the side chain of Arg21 and the main chain of Pro44 further stabilizes the dimer interface, in addition to nonpolar interactions from multiple residues (e.g., Val5, Ile7, Val10, Leu14, Leu15, Leu18, Phe32, Leu33, Leu34, and Leu37).

The two dimers interact mainly through a zinc metal ion coordinated by Asp12 and His16 from helix α1 of each dimer, with an average distance of 2.03 Å (Figure 2b). The residue Arg26 from the dimer forms a salt bridge with Glu13 from the adjacent dimer in the crystal lattice. The electrostatic surface of the dimer showed a positive charge on one side and a negative charge on the other side (Figure 2c and 2d). Residues Arg8 (β1-strand), Lys19 (α1-helix), and Arg26 (α2-helix) contribute to the positive charge, while residues Asp31, Glu39, Glu42, Glu43, and Glu46 (α2-helix) and Glu17 (α1-helix) contribute to negative charge. The crystal structures of toxin-antitoxin complexes with DNA (e.g., Arc, MetJ, and CopG) showed an anti-parallel β-sheet from the antitoxin dimer that mediates interactions with DNA by inserting the β-sheet into the major groove of DNA[35–37]. Structural comparison of VapB12 dimers with antitoxin DNA complexes suggests that Arg8 and Qln6 likely mediate interactions with DNA.

Dimerization of VapC12 is essential for its activity

AlphaFold was used to predict the structure of the TA complex and generate the structure of the VapC12 toxin (Figure 3a and 3b). Through computational modeling, we identified that VapC12 forms a homodimer via the tryptophan residue at the 74th position. To verify this, we expressed His-tagged versions of wild type and tryptophan mutated ($W_{74}G$) VapC12 separately in an *E. coli* expression system.

Western blot analysis of the recombinant protein revealed that, unlike the wild type, the dimer form of the VapC12 toxin was completely absent from the toxin harbouring the $W_{74}G$ point mutation (Figure 3e). Additionally, using the *M. smegmatis* growth model, we also demonstrated that the oligomerization of the toxin is essential for its activity (Figure 3f). In sum, our data suggest that W74 residue is critical for the homo-dimerization of toxin which is essential for its ribonuclease activity.

VapC12 interact with VapB12 through CRAC motif

We aligned and analyzed the protein sequences of PIN domain-containing prokaryotic proteins. Intriguingly, the VapC12 protein has a sequence that bears the signature of the CRAC motif known to recognize and bind to cholesterol. This unique motif is exclusively present in the VapC12 toxin specific to mycobacteria (Figure S4). Using a computational approach, we constructed the VapBC12 TA complex, which was validated by post-model analysis for further *in-silico* studies. While multiple structural hypotheses were considered, it was through our integrative computational strategy that we were able to predict the binding mode and orientation of the antitoxin relative to the toxin. Notably, our model revealed interaction of the C-terminal tail of the anti-toxin with a specific groove present in the toxin that overlaps with the CRAC motif (Figure 3c and 3d). The binding conformation identified via *in-silico* analysis provides new mechanistic insight into the molecular basis of toxin-antitoxin interaction. To confirm if the CRAC motif is involved in dimerization of the toxin, we mutated one of the critical residues of the CRAC motif ($F_{66}L$) and heterologously expressed it in *E.coli*. No variations were seen in the formation of a homodimeric band between the $F_{66}L$ mutant and the wild type, as shown by western blot analysis (Figure 3e, down). Furthermore, $F_{66}L$ mutation did not affect the activity of the toxin (Figure 3f). Subsequently, we aimed to validate the function of the CRAC

motif in the interaction of the VapBC12 TA system. To this end, we employed protein-protein interaction analysis utilizing the M-PFC assay [38]. where we cloned toxin (VapC12) in the bait vector and antitoxin (VapB12) in the prey vector. The assay used known mycobacterial interacting partners, ESAT-6 and CFP10, and the vector alone as positive and negative control, respectively (Table S2). Interaction between bait and prey proteins would result in complete murine-dihydrofolate reductase (mDHFR), which confers resistance to trimethoprim (trim). We observed resistant colonies in the WT-VapBC12 TA group, However, mutated toxin ($VapC12^{F66L}$) failed to interact with VapB12 as evident by growth depletion on the trim-supplemented plate (Figure 3g). To check the biological implication of the above substitution ($F_{66}L$), we generated overexpressing vectors with both toxin and anti-toxin as an operon in one vector (WT-VapBC12) and mutated only the toxin in this vector ($VapBC12^{F66L}$). On electroporation of these vectors in *M. smegmatis,* we observed that the co-expression of the anti-toxin failed to rescue the toxin-mediated growth defect in the toxin-mutated strain (Figure 3h). The above data suggest that F66 in the toxin is not involved in homo-dimerization but is essential for binding and neutralization of the toxin activity.

Structure-function analysis of VapBC12 TA system

For a detailed structural functional analysis of the VapBC12 TA system inside the pathogen, we generated strains of *M. smegmatis* harboring different versions of the TA gene pairs with specific mutations. We used the above M-PFC assay to study PPI. Substituting tryptophan 74 with glycine ($W_{74}G$) in the toxin reduced its binding affinity to VapB12 anti-toxin (Figure 4a, trim plate). This mutation prevents the toxin from forming a homodimer essential for its activity (Figure 4a, bar graph). This indicates that oligomerization of the toxin is critical for both the stability of the TA

complex as well as the activity of the toxin. Further, the substitution of Histidine to alanine at position 16 in VapB12 anti-toxin ($H_{16}A$), predicted to be critical for Zn ion-mediated oligomerization of the anti-toxin, negatively affected the interaction of the toxin with the anti-toxin as indicated by PPI data (Figure 4b, trim plate). The growth analysis of strain expressing VapBC12 harboring this mutation emphasized that the oligomerization of the antitoxin is critical for the maintenance of the integrity of TA structure, failing which, the toxin attains a constitutively active form that results in growth arrest (Figure 4b, bar graph). To confirm the role of Zn ion in TA binding dynamics, we performed the PPI and the *M. smegmatis* growth experiment in both with and without Zn-containing media using the wild-type version of the VapBC12 expression construct. Interestingly, the data suggest that the binding of the VapC12 toxin to the VapB12 antitoxin was completely dependent on the presence of Zn ion in the media (Figure 4c and 4d, trim plate). The same was further validated using the *M. smegmatis* growth model experiment, wherein, the overexpression of wild type TA protein complex in *M. smegmatis* did not show any growth inhibition in the presence of Zn (Figure 4c, bar graph) while a significant reduction was observed on Zn-depleted media (Figure 4d, bar graph). The above findings suggest that the W_{74} residues of the toxin and the H_{16} residue of the anti-toxin are essential for both the structural integrity of the VapBC12 complex and regulation of the VapC12 ribonuclease activity.

Competitive displacement of VapB12 anti-toxin by cholesterol activates VapC12 toxin

Using an in-silico approach, we demonstrated that cholesterol docks perfectly in the anti-toxin binding groove created by the CRAC motif of the toxin (L_{60}-R_{72}) (Figure 5a-b and 3c-d). This suggests that cholesterol may displace anti-toxin from the CRAC

motif of the toxin. We checked this hypothesis with the M-PFC PPI assay. This experiment demonstrated that, unlike glycerol, the presence of cholesterol in the media restricted the binding of the VapB12 anti-toxin to the cognate VapC12 toxin (Figure 5c). Interestingly, the co-expression of VapB12 anti-toxin failed to rescue the growth of *M. smegmatis* overexpressing the VapC12 toxin in the presence of cholesterol, while it effectively restored the phenotype on glycerol and oleate media (Figure 5d). A concentration-dependent growth inhibition by cholesterol in the strain expressing both toxin and antitoxin further confirms the hypothesis. Overall, the data support our hypothesis that the antitoxin and cholesterol binding sites overlap at the CRAC motif of the toxin and that the dose-dependent competitive displacement of the antitoxin by cholesterol results in the activation of the ribonuclease activity of the VapC12 toxin.

Generation and selection of Antitoxin mimicking peptides

Computational studies were carried out to generate five peptides (9 to 13 mer). from interacting interface of the VapBC12 TA complex. The interaction pattern of diverse-length peptides from VapB12 was characterized using protein-peptide docking with VapC12 for each peptide. Furthermore, the best complexes of peptide and toxin were used to perform the thermodynamic quantification by applying the Molecular Mechanics-Generalised Born Surface Area (MM-GBSA) approach (Figure 6a). Based on interaction fingerprinting and MM-GBSA score, the peptide of 11 amino acids (P2) has shown the best energy (-44.6 kcal/mol) and a cooperative electrostatic complementarity (Figure 6b). P2 was identified to tuck well and interact with the CRAC motif of VapC12 toxin. Therefore, P2 was chosen for further studies. To understand the binding dynamics of cholesterol and P2 peptide to the CRAC motif of the VapC12 toxin, we performed molecular docking simulation analysis. The

docked and bound states of cholesterol and P2 (L_{50}-D_{60}), respectively, reveal that they occupy the same site and align well in the binding pocket with a binding energy of -43.1 kcal/mol and -44.6 kcal/mol, respectively (Figure 6c). The cluster representative of cholesterol and antitoxin simulating peptide was chosen for MD simulation studies (Figure 6d and 6h). Cholesterol was lined by 17 residues while the peptide was lined by 19 residues, out of which 9 residues were common. These residues were L4, L12, L14, T15, G28, V31, V63, F66 and L67 (Figure 6e and 6i). After observing the binding pattern, we wanted to understand their specific interaction with the CRAC motif residues. Interestingly, both the cholesterol and P2 peptide interact with 5 residues of the CRAC motif, but are not completely the same. Cholesterol interacted with V61, V63, N65, F66 and L67 while Peptide interacted with V62, V63, F66, L67 and L69 (Figure 6g and 6j). The above study revealed that both cholesterol and peptide fit well and are deeply embedded in the binding pocket which justifies their stability (Figure 6c-j). This competitive but differential binding pattern of cholesterol and P2 peptide was hypothesized to result in an open and closed state of the catalytic PIN domain through which the toxin performs its ribonuclease activity. The P2 peptide was thus chemically synthesized for *in-vitro* validations.

VapC12 toxin inhibition potentiates the activity of the anti-TB drugs

To evaluate the ability of P2 peptide to inhibit the VapC12 activity, we performed a concentration-dependent increase in the luminescence in our *M. smegmatis*-based model. The concentration-dependent rescue of the toxin-expressing *M. smegmatis* was measured in terms of an increase in the luminescence intensity on both glycerol (Figure 7a) and cholesterol (Figure 7b) media. As expected, relative to glycerol, we observed a 4- fold higher requirement of the anti-toxin mimicking peptide in

cholesterol for the rescue of the toxin-expressing *M. smegmatis* culture. However, the effective peptide concentration was significantly lower when tested on *M. tuberculosis* due to the relatively lower sensitivity of *M. tuberculosis* than *M. smegmatis* (Figure S5e). Inquisitively, we also checked whether the peptide-mediated growth enhancement alter drug susceptibility profile of *M. tuberculosis*. We performed the antibiotics killing assay using 10X MIC concentration of anti-TB drugs with and without the VapB12 mimicking peptide (P2). We named this peptide "anti-persister" because it inhibits the formation of *M. tuberculosis* persister population, evident by better growth on peptide treatment in cholesterol media (Figure 7e). Interestingly, we did not observe similar phenotype in glycerol media (Figure 7f), which again validated the cholesterol-specific activity of VapC12 and neutralization by P2 peptide, consequently sensitizing *M. tuberculosis* to first and second-line anti-TB drugs. The cholesterol-specific phenotype could be reflected in the THP-1 infection model (Figure 7g). Moreover, we observed a time-dependent linear killing when peptide was added in rifampicin group in contrast to rifampicin-only group, suggesting that the peptide can reduce the generation of the drug-tolerant persister population in *M. tuberculosis* (Figure S6b). Overall, our observations indicate that the P2 peptide effectively suppressed persister development in *M. tuberculosis* and enhanced the efficacy of anti-TB drugs.

Discussion

The stochastic generation of drug-tolerant persisters, coupled with the ability of *M. tuberculosis* to persist within hosts for extended periods, poses a significant challenge to effective tuberculosis treatment and necessitates prolonged treatment regimens[1–4]. The increased prevalence of immunocompromised individuals coupled with an increase in the frequency of drug-resistant tuberculosis cases, makes

treating this disease even more challenging[39,40]. A treatment regimen for latent TB infection exists[39,40]. However, there is no clinically available drug to target the persister population of mycobacteria. Recent studies have shown that inhibition of the trehalose catalytic shift[4], blocking stringent response by hyperphosphorylated guanosine[41], repression of dihydrolipoamide acyltransferase (DlaT)[42], an enzyme required to resist nitric oxide-derived reactive nitrogen intermediates, or targeting the cytoplasmic membrane[43,44] reduces the persister population, resulting in enhanced effectiveness of first-line and second-line anti-TB drugs in macrophage infection models. While these compounds directly kill the persister population, inhibitory molecules that target the modulatory pathways involved in persister formation are yet to be explored. Host innate factors, such as cholesterol and other lipids, are important determinants of the mycobacterial phenotype within infected cells[5,28]. Targeting triacylglycerol synthesis in the host mitigates *M. tuberculosis* persistence, and thus results in better clearance in the presence of antibiotics[5]. Several studies have also suggested that targeting the cholesterol metabolism pathway of *M. tuberculosis* may offer a promising therapeutic approach against tuberculosis[45–47].

Previous studies from our group have demonstrated that cholesterol-mediated modulation of mycobacterial growth and pathogenicity within the host is dependent on VapC12 toxin [28–30]. VapC ribonuclease toxins from type II TA systems in *M. tuberculosis* are usually activated upon the dissociation and subsequent degradation of their cognate antitoxins. Antitoxin usually possesses intrinsically flexible domains susceptible to proteolysis which is mitigated by a strong binding of the toxin. While some proteases responsible for anti-toxin degradation have been identified[22,48–50], the specific dissociation signals that trigger selective proteolysis remain poorly

understood. In this study, we employed a multifaceted approach to elucidate the mechanism underlying cholesterol-mediated dissociation of VapB12 and further activation of VapC12 toxin in *M. tuberculosis*. Furthermore, as a proof-of-concept, we successfully demonstrated that inactivation of the VapC12 toxin by the synthetic peptide designed from VapB12 groove based on interaction mapping and protein-protein interaction analysis. The most potent peptide (P2) is able to bind to the CRAC motif of VapC12, potentiates the activity of first and second-line anti-TB drugs.

Our findings corroborate a previous study demonstrating the importance of the hydrophobic core in VapC homo-dimerization [51]. Consistent with the structural analysis of type II TA systems in various pathogen[23,24,52], we predict that the VapBC12 TA system forms a hetero-octamer, which is crucial for toxin neutralization. While divalent metal ions (Mg^{2+}, $Mn^{2+,}$ and Ca^{2+}) are known to be essential for the catalytic activity of toxin ribonucleases in several VapBC TA systems [19,24,51], their role in the stability of the TA system remains unclear. We report for the first time that the anti-toxin VapB12 forms a homotetramer through Zn^{2+} metal ion binding to stabilize the TA hetero-octameric complex. The metal-binding residues (Aps12 and His16) appear unique to VapB12, as they are not conserved in structural homologs identified by the Dali search (Figure S2B). The physiological binding of this antitoxin tetramer to the TA promoter is yet to be explored.

Cholesterol recognition amino acid consensus (CRAC) motifs, which enable cholesterol binding, are common in eukaryotic membrane proteins (e.g., GPCRs) and viral entry proteins[53,54]. These motifs are also found in some bacterial toxins, like alpha-hemolysin, where they are essential for cholesterol binding and pathogen toxicity[55]. In the current study, we report the presence of a CRAC motif overlapping

with the antitoxin binding site in the VapC12 toxin. Our data further suggest that, while binding of the antitoxin to the CRAC motif neutralizes the effect of the toxin, displacement of the antitoxin by cholesterol activates VapC12 ribonuclease activity. However, insights at the molecular level are required to validate this theory.

Contrary to the paradigm of TB research that focuses on the development of antimicrobial peptides that activate toxins, we, to the best of our knowledge, are the first ones to demonstrate that a peptide that inactivates VapC12 toxin activity and thus works as an inhibitor of persister formation in *M. tuberculosis*, enhanced the effectiveness of anti-TB drugs (Figure 8). Thus, such peptide or small molecules mimicking these peptides hold promise to be evaluated as adjunct in combination with extant TB drugs for the treatment of tuberculosis. Nonetheless, the peptide concentration is too high to be used in an *in-vivo* infection model. We are now focused on peptide modulations and the screening of small compounds for in-vivo testing.

In Conclusion, the presented strategy ought to overcome the major Achilles' heel of efficient TB treatment regimens. The role of VapBC12 TA system in growth modulation leading to the generation of persisters underscores the importance of targeting this TA system against the formation of persisters during *M. tuberculosis* infection. Collectively, we identified and demonstrated the mechanism of cholesterol-mediated generation of persisters during *M. tuberculosis* infection and as a proof-of-concept demonstrated that targeting persisters as an adjunct therapy could potentiate and help shorten the existing regimen.

Materials and Methods

Bacterial strains and growth conditions.

M. smegmatis mc^{2}155 and *M. tuberculosis* strains were cultured on Middlebrook 7H9 broth (Difco, BBL]. Bacterial enumeration was done on 7H11 (Difco, BBL) agar plates supplemented with OADS for *M. tuberculosis*, and colonies were counted after 4 days for *M. smegmatis* and 21 days of incubation for *M. tuberculosis*. When necessary, Middlebrook medium was supplemented with KAN (25 µg/ml) (Sigma) , HYG (50 µg/ml) (Sigma), or TRIM (50 µg/ml) (Sigma) and ATc (400 ng/ml) (Caymen), unless otherwise stated. *E. coli* XL1 blue and BL21 (DE3) strain was grown in Luria Bertani Agar, Miller [catalog no. M1151-500G] and Luria Bertani Broth [catalog no. M1245-500G] supplemented with KAN (50 µg/ml) or HYG (150 µg/ml). Strains and primers used in this study are listed in Tables S2, S3, and S4, respectively.

Replication Kinetics studies

The wild-type and VapC12-deleted *M. tuberculosis* strains were transformed with a "molecular clock" plasmid, pBP10 [gift of D. Sherman[33], which is released from replicating bacteria in the non-selective media. The plasmid loss in the absence of the selection marker allows a direct measurement of replication, calculated as the ratio of plasmid-carrying bacteria divided by the total number of bacteria. The VapC12 Comp strain was not used in this assay due to a conflict with the selectable markers. Log phase cultures of both strains grown in kan-supplemented Middlebrook 7H9 broth were washed with phosphate-buffered saline plus 0.05% tyloxapol (Sigma) (PBST) to remove remaining nutrients. These washed cultures were used to set an OD of 0.01 in minimal media supplemented with 0.1% glycerol (Sigma), referred as glycerol media, 150µM cholesterol (Sigma), referred as cholesterol media. The minimal media was also supplemented with 0.05% tyloxapol (Sigma) to prevent clumping, which could affect the accuracy of the bacterial counts. The

optimal dilutions of the cultures were plated on 7H11-agar plate supplemented with and without kanamycin (30 mg/ml) to assess replication rates and growth, respectively. The following formula was used to determine the plasmid retention represented by pBP10+ cells of the two strains in different media:

% pBP10+ cells = CFU on Kan-supplemented plate/CFU on plain plate *100

Growth curve studies

For experiments related to *M. smegmatis* models, Log-phase cultures of wild-type *M. smegmatis* mc^2155, VapC12, VapB12, and VapBC12 overexpressing strains were washed with 1X PBST and inoculated in 7H9 media supplemented with 0.01% tween 80 (Sigma) and minimal media supplemented with 0.1% glycerol, 150µM cholesterol and 200 µM oleic acid media, at an absorbance of 0.001. Aliquots of the cultures were obtained at different time points and luminescence was recorded in a 96-well white plate using SpectraMax iD3 Multi-Mode Microplate Readers and optimal dilutions were prepared to be plated on 7H11 agar plates for bacterial enumeration.

SDM (Site Directed Mutagenesis) generation

The SDMs in the *vapC12* gene, wherein phenylalanine (F66) and tryptophane (W74) were mutated to leucine (L66) and glycine (G74) and the vapB12 gene where histidine (H16) was mutated to alanine (A16), were generated by DpnI enzyme (NEB) treatment. Mutants were generated in the constructs containing individual VapB12 or VapC12 and both VapBC12 together cloned in one plasmid as an operon. The cloned constructs were used as a template for PCR amplification using SDM primers listed in Table S4. The PCR product was PCR purified and treated with DpnI enzyme for 4 h at 37°C. No-template and no-DpnI-treatment control samples were also maintained. All the reactions were transformed in E. coli XL-1 Blue-

competent cells. The constructed products were sequenced and electroporated in *M. smegmatis* -competent cells for further studies.

Chemical cross-linking

The vector pET28a was used for the expression of His6-VapC12 in E. coli (DE3) strain. The SDM mutant (W74G) was generated using Dpn1 digestion technique as stated above. The overnight culture was inoculated into 10 mililiter of fresh LB media (1:100) supplemented with 100mg/ml of kanamycin and allowed to grow until the OD_{600} reached between 0.6-0.8. The culture was then induced with 1 mM IPTG (isopropyl-β-D-thiogalacto-pyranoside) (Sigma) and allowed to grow at 37°C for 4 hours with vigorous shaking (120 rpm) before harvesting cells (6 min, 10,000 rpm) and resuspension in 50 mM Tris (pH 8.0), 500 mM NaCl, 5 mM MgCl2, 5 mM β-mercaptoethanol, 10 mM imidazole (Sigma). Cells were disrupted by sonication on ice with 30% amplitude and pulses of 10s : 10s (i.e. energy for 10s followed by a pause for 10s) for about 2 min. Protein lysates were collected from wt and mutated strains and given a treatment of 0.001% of chemical cross-linker, glutaraldehyde for 5 min before preparing the sample in Laemmli buffer by boiling at 95^0 Celsius, separated on a 12% SDS-polyacrylamide gel and analyzed with western blot using his-tagged antibody.

Mycobacterial Protein Fragment Complementation (M-PFC)

The plasmids pMD101 and pMD102 (Kindly provided by Dr. Ashwani Kumar, CSIR-IMTECH, India) containing mDHFR-F(1, 2) and mDHFR-F(3), respectively, were used as vector to clone VapC12 (toxin) as bait and VapB12 (anti-toxin) as prey protein. SDMs were generated separately in cloned constructs of toxin and anti-toxin using the primers listed in Table S4. F66L and W74G in toxin and H16A in antitoxin. Protocol for *M. smegmatis* culturing were used as described previously[40].Briefly, *M.*

smegmatis cells were independently transformed with M-PFC plasmids producing [F1,2]/F3] as negative control, Esat-6[F1,2]/Cfp-10[F3] as positive control, and VapC12[F1,2]/VapB12[F3], VapC12:F66L [F1,2]/VapB12[F3], VapC12:W74G [F1,2]/VapB12[F3] VapC12[F1,2]/VapB12:H16A[F3] (Table S2). The transformants were streaked onto a 7H11 medium containing Trimethoprim 50µg/ml along with positive and negative control. The streaked plate was incubated at 37°C. The plates were observed for growth after 4 days.

VapBC12 expression and protein purification

VapB12 (Rv1721c) and VapC12 (Rv1720c) were expressed and purified as described earlier[24]. Briefly, the two genes were cloned separately into pET28a and transformed into BL21 (DE3). The transformed cells were grown overnight, and the culture was inoculated in 1 liter of new LB medium (1:100) supplemented with 100 mg/ml of kanamycin and allowed to grow until the OD_{600} reached 0.6. After that, the culture was induced with 1 mM IPTG and let to grow at 37°C with 120 rpm shaking overnight. Cultured bacteria were harvested by spinning at 6,000 *g for 10 min and checked for expression by SDS-PAGE. Majority of the VapC12 (Rv1720c) protein was found as inclusion bodies (IBs) in the pellet. Using sonication and many washing stages, pure IBs carrying rRv1720c were isolated. In brief, one milliliter of pure rRv1720c IBs was dissolved in nine milliliters of buffer (50 mM Tris-HCl [pH 8.0], 300 mM NaCl, 10 mM β-mercaptoethanol, and 8 M urea) and let stand for an hour at room temperature. The sample was then centrifuged at 15,000*g for twenty minutes at 10°C. The obtained supernatant was used to purify recombinant VapC12 protein by immobilized metal ion affinity chromatography using a HisTrap FF column (GE Healthcare Buckinghamshire, UK) under denaturing conditions Protein was eluted using buffer (50 mM Tris-HCl [pH 8.0], 300 mM NaCl, 10 mM β-mercaptoethanol, 8

M urea, and 250 mM imidazole). Denatured purified protein was refolded by dilution in a pulsatile manner at 4°C while being constantly stirred in a refolding buffer (100 mM phosphate buffer [pH 6.4], 300 mM NaCl, and 5 mM β-mercaptoethanol). The refolded target protein sample was centrifuged at 24,000 g for thirty minutes at 4°C. The supernatant including the refolded active protein, was then concentrated and dialyzed three times against the buffer, which consisted of 100 mM phosphate buffer [pH 6.4], 300 mM NaCl, and 5 mM anhydroethanol. The protein's final buffer exchange was carried out using a PD10 desalting column (GE Healthcare Buckinghamshire, UK) using the following parameters: 100 mM phosphate buffer [pH 6.4], 300 mM NaCl, and 10% glycerol. VapB12 (Rv1721c) was purified from the supernatant of lysed-induced cultures using a HisPur Cobalt purification kit (3 ml; Thermo Scientific, catalog no. 90092). Proteins were quantitated by a bicinchoninic acid assay (Thermo Scientific Pierce, Rockford, IL), analyzed and confirmed by SDS-PAGE and Western blotting with anti-His monoclonal antibody (Cell Signaling Technology, Inc., Danvers, MA).

Crystallization and structure determination

The toxin (VapC12) and antitoxin (VapB12) were mixed at an equimolar ratio and incubated at 4°C for an hour with gentle shaking. The toxin-antitoxin complex sample was then concentrated to 900 µL, centrifuged at high speed to remove any precipitates, and injected into a HiLoad 16/60 Sephacryl S100 HR (Cytiva) size-exclusion chromatography (SEC) column. The eluted protein fractions were combined, concentrated to 3 mg/ml, and subjected to crystallization trials. Crystallization screenings of the VapBC12 complex were performed at 22°C using the sitting-drop vapor-diffusion technique with an automated liquid handling robotic system (Mosquito, TTP Labtech) against various commercial screening solutions.

Protein crystals appeared in a few conditions, with poor diffraction quality. The initial conditions were subsequently reproduced and optimized by hanging-drop vapor-diffusion method using hanging-drop vapor diffusion method by mixing sample and reservoir solution in a 1:1 ratio for making 2 µl drop and equilibrating it against 1000 µl reservoir solution. A condition containing 0.2 M ammonium chloride-NaOH pH 6.3 and 20% (w/v) PEG 3350 produced diffraction-quality crystals after two weeks (Supplementary Figure 2).

Preliminary X-ray diffraction analysis and screening were performed at the home source with a Xenocs GeniX3D Cu (high-flux) microbeam X-ray generator and a MAR 345 image-plate detector (MAR Research). High-resolution diffraction data were collected at the synchrotron beamline ID29 (ESRF synchrotron facility at Grenoble, France) (Table 1) using 30% ethylene glycol as a cryoprotectant. Diffraction data were indexed and integrated with *XDS* [56] and scaled using *AIMLESS* [57] in the *autoPROC* package [58]. The crystals diffracted to 1.6Å resolution and belonged to the tetragonal space group $P4_1$, with unit cell parameters of a = 34.66 Å, b = 34.66 Å, c = 162.23 Å, and α = β = γ = 90.00°.

Initial attempts to determine the phases via molecular replacement using the related VapBC structures were unsuccessful. Fortunately, significant anomalous signals were observed during data processing, likely from zinc bound to the protein. We then proceeded with phase determination and preliminary model building via single-wavelength anomalous dispersion (SAD) phase calculation using ShelxCDE [59]. Subsequent model building with phenix.autobuild [60] and the final model refinement cycles through an iterative process utilizing Refmac [61] and Coot were performed within the CCP4 [62]. The refinement process included an initial round of rigid-body refinement, followed by subsequent cycles incorporating TLS parameters determined

via the TLSmd server[63]. The final refined model of VapB12 exhibited Rwork/Rfree values of 0.172/0.218, showing excellent geometric properties, with no residues falling within the disallowed regions of the Ramachandran Plot. The final model revealed only the antitoxin (residues 1-44), and its C-terminal region (residues 45-75) was likely lost during crystallization. After validation, the coordinates of the final model were deposited in the Protein Data Bank (PDB) with accession number (PDB-ID:7E4J).

Molecular docking of Cholesterol

The focused docking[64,65] of cholesterol was performed by taking the centroid of the residues of CRAC motif residues. The molecular docking was performed using AUTODOCK4.2 [66,67]. The most likely pose was selected for energy minimization using molecular dynamics simulation to avoid any bad contacts [68].

Free energy analysis through MM-GBSA (molecular mechanics/ generalized born surface area). The average binding energy was calculated by:

$\Delta Gbind = \Delta EMM + \Delta Gsolv + \Delta GSA$

Where the difference in the minimized energies between ligand and protein complexes is denoted by ΔE_{MM}. ΔG_{solv} is the difference in the GBSA solvation energy of the complexes and sum of solvation energies for the protein and ligand, whereas the differences in surface area energy of the complex and sum of that in protein and ligand[69].

Interaction map-based peptide designing and docking

VapB12 residues that were crucial for binding within the CRAC motif of VapC12 were identified based on interaction types obtained from the VapBC12 (TA) interface, which was then utilized for peptide formation. Based on interacting

interface the diverse lengths of five peptides were identified from the TA interface. Furthermore, peptide-protein docking was carried out using HDOCK (standalone) to get the best pose of all peptides. Furthermore, to get the quantitative values the MM-GBSA of each complex was carried out to get the free energy of binding.

Statistics and reproducibility

The data values are represented as mean ± SD of the replicates from two to three independent experiments. Wherever applicable, the number of replicates per group has been indicated by the dots. GraphPad Prism (ver 9.0) has been used for the statistical analysis of all data with suitable statistical tests. Statistical comparisons with *p-values* are mentioned in the respective figure legends.

Acknowledgements

The authors acknowledge THSTI for infrastructural support, BSL-3 facility (and staff) for all *M. tuberculosis*-related experiments. Technical support of Mr Sharad Dwivedi for experimental work is duly acknowledged. We are grateful for Dr Vaibhav Kumar Nain's technical assistance in giving critical editing for the figures and legends. We also duly acknowledge the receipt of plasmids and constructs used in the study (Supplementary Information). This study was supported by the grant (No. EM/Dev/SG/212/7864/2023) from the Indian Council of Medical Research (ICMR), Government of India, and intramural funding by BRIC-THSTI to A.K.P. and is duly acknowledged. Z.H. was supported by the research fellowship from DBTHRDPMU/JRF/BET-21/1/2021-22/236. V.K. acknowledge RCB for the in-house X-ray, central instrumentation facilities and the beamline scientist Dr. Nicolas FOOS at ESRF for the support during the data collection, and the DBT-EMBL partnership

program for providing access to the ESRF synchrotron facility. D.S. and S.A. acknowledge NNP grant (NNP-BT/PR40189/BTIS/137/50/2022) and DBT-TRP grant, respectively.

Data availability:

Structural coordinates for the VapB12 antitoxin have been deposited in the Protein Data Bank with ID: 7E4J.

Author information

These authors contributed equally: Shivendra Pratap Singh, Sakshi Talwar.

Authors and Affiliations

Mycobacterial Pathogenesis Laboratory, Centre for Tuberculosis Research, BRIC-Translational Health Science and Technology Institute, Faridabad, Haryana, India

Zohra Hashmi, Sakshi Talwar, Taruna Sharma & Amit Kumar Pandey

Special Centre for Molecular Medicine, Jawaharlal Nehru University, New Delhi, India

Zohra Hashmi, Sakshi Talwar & Taruna Sharma

Computational Biophysics and CADD Group, Computational and Mathematical Biology Centre, BRIC-Translational Health Science and Technology Institute, Faridabad, Haryana, India

Mitul Srivastava, Debapriyo Sarmadhikari & Shailendra Asthana

Lab of Structural Microbiology, Regional Centre of Biology, Faridabad, Haryana, India

Shivendra Pratap Singh, Abhin Kumar Megta, Vengadesan Krishnan

Contributions

Z.H., S.T., A.K.P. designed the research; Z.H., S.T., T.S. performed the microbiology-based experiments; C.S. performed the protein purification expts; S.P.S. and A.K.M. performed crystallography-related experiments; M.S, D.S. and S.A. performed computational studies. Z.H., S.P.S., S.A., K.V., and A.K.P. analysed the data. Z.H. and A.K.P. drafted the manuscript. All authors contributed to the manuscript revision. A.K.P.: overall supervision.

Corresponding authors

Correspondence to Shailendra Asthana, Krishnan Vengadesan, and Amit Kumar Pandey.

Competing interests

The authors declare no competing interests.

References

1. Global Tuberculosis Programme. https://www.who.int/teams/global-tuberculosis-programme/the-end-tb-strategy.
2. Balaban, N. Q., Merrin, J., Chait, R., Kowalik, L. & Leibler, S. Bacterial persistence as a phenotypic switch. *Science* **305**, 1622–1625 (2004).
3. Bhaskar, A., Dwivedi, V. P. & Nandicoori, V. K. Eliminating Mycobacterial Persistence: Novel Targets for Anti-TB Therapy. in *Pathogenicity and Drug Resistance of Human Pathogens: Mechanisms and Novel Approaches* (eds. Hameed, S. & Fatima, Z.) 57–79 (Springer, Singapore, 2019). doi:10.1007/978-981-32-9449-3_3.
4. Kalera, K. *et al.* Targeting Mycobacterium tuberculosis Persistence through Inhibition of the Trehalose Catalytic Shift. *ACS Infect. Dis.* **10**, 1391–1404 (2024).

5. Kalam, H. *et al.* Identification of host regulators of Mycobacterium tuberculosis phenotypes uncovers a role for the MMGT1-GPR156 lipid droplet axis in persistence. *Cell Host Microbe* **31**, 978-992.e5 (2023).
6. Goossens, S. N., Sampson, S. L. & Van Rie, A. Mechanisms of Drug-Induced Tolerance in Mycobacterium tuberculosis. *Clin. Microbiol. Rev.* **34**, e00141-20 (2020).
7. Co, D. O., Hogan, L. H., Kim, S.-I. & Sandor, M. Mycobacterial granulomas: keys to a long-lasting host–pathogen relationship. *Clin. Immunol.* **113**, 130–136 (2004).
8. Ehrt, S. & Schnappinger, D. Mycobacterial survival strategies in the phagosome: defence against host stresses. *Cell. Microbiol.* **11**, 1170–1178 (2009).
9. Baker, J. J., Johnson, B. K. & Abramovitch, R. B. Slow growth of Mycobacterium tuberculosis at acidic pH is regulated by phoPR and host-associated carbon sources. *Mol. Microbiol.* **94**, 56–69 (2014).
10. Gerdes, K. Toxin-antitoxin modules may regulate synthesis of macromolecules during nutritional stress. *J. Bacteriol.* **182**, 561–572 (2000).
11. Barry, C. E. *et al.* The spectrum of latent tuberculosis: rethinking the biology and intervention strategies. *Nat. Rev. Microbiol.* **7**, 845–855 (2009).
12. Baker, J. J. & Abramovitch, R. B. Genetic and metabolic regulation of Mycobacterium tuberculosis acid growth arrest. *Sci. Rep.* **8**, 4168 (2018).
13. Agarwal, S. *et al.* VapBC22 toxin-antitoxin system from Mycobacterium tuberculosis is required for pathogenesis and modulation of host immune response. *Sci. Adv.* **6**, eaba6944 (2020).
14. Kumar, A. *et al.* Toxin-Antitoxin (TA) Systems in Stress Survival and Pathogenesis. in *Mycobacterium Tuberculosis: Molecular Infection Biology,*

Pathogenesis, Diagnostics and New Interventions (eds. Hasnain, S. E., Ehtesham, N. Z. & Grover, S.) 257–274 (Springer, Singapore, 2019). doi:10.1007/978-981-32-9413-4_15.

15. sundaram, K., Vajravelu, L. K. & Paul, A. J. Functional characterization of toxin-antitoxin system in *Mycobacterium tuberculosis*. *Indian J. Tuberc.* **70**, 149–157 (2023).
16. Ahidjo, B. A. *et al.* VapC Toxins from Mycobacterium tuberculosis Are Ribonucleases that Differentially Inhibit Growth and Are Neutralized by Cognate VapB Antitoxins. *PLoS ONE* **6**, e21738 (2011).
17. Winther, K., Tree, J. J., Tollervey, D. & Gerdes, K. VapCs of Mycobacterium tuberculosis cleave RNAs essential for translation. *Nucleic Acids Res.* **44**, 9860–9871 (2016).
18. Mycobacterium tuberculosis VapC4 toxin engages small ORFs to initiate an integrated oxidative and copper stress response | PNAS. https://www.pnas.org/doi/full/10.1073/pnas.2022136118.
19. Das, U. *et al.* Crystal structure of the VapBC-15 complex from Mycobacterium tuberculosis reveals a two-metal ion dependent PIN-domain ribonuclease and a variable mode of toxin-antitoxin assembly. *J. Struct. Biol.* **188**, 249–258 (2014).
20. Deep, A., Kaundal, S., Agarwal, S., Singh, R. & Thakur, K. G. Crystal structure of Mycobacterium tuberculosis VapC20 toxin and its interactions with cognate antitoxin, VapB20, suggest a model for toxin-antitoxin assembly. *FEBS J.* **284**, 4066–4082 (2017).
21. Jardim, P., Santos, I. C. da S., Barbosa, J. A. R. G., de Freitas, S. M. & Valadares, N. F. Crystal structure of VapC21 from Mycobacterium tuberculosis at 1.31 Å resolution. *Biochem. Biophys. Res. Commun.* **478**, 1370–1375 (2016).

22. Loris, R. *et al.* Crystal structure of the intrinsically flexible addiction antidote MazE. *J. Biol. Chem.* **278**, 28252–28257 (2003).
23. Maté, M. J. *et al.* Crystal structure of the DNA-bound VapBC2 antitoxin/toxin pair from Rickettsia felis. *Nucleic Acids Res.* **40**, 3245–3258 (2012).
24. Min, A. B. *et al.* The crystal structure of the Rv0301-Rv0300 VapBC-3 toxin-antitoxin complex from M. tuberculosis reveals a Mg^{2+} ion in the active site and a putative RNA-binding site. *Protein Sci. Publ. Protein Soc.* **21**, 1754–1767 (2012).
25. Deep, A. *et al.* Structural, functional and biological insights into the role of Mycobacterium tuberculosis VapBC11 toxin–antitoxin system: targeting a tRNase to tackle mycobacterial adaptation. *Nucleic Acids Res.* **46**, 11639–11655 (2018).
26. Lee, I.-G. *et al.* Structural and functional studies of the Mycobacterium tuberculosis VapBC30 toxin-antitoxin system: implications for the design of novel antimicrobial peptides. *Nucleic Acids Res.* **43**, 7624–7637 (2015).
27. Freire, D. M. *et al.* An NAD+ Phosphorylase Toxin Triggers Mycobacterium tuberculosis Cell Death. *Mol. Cell* **73**, 1282-1291.e8 (2019).
28. Mycobacterial persistence requires the utilization of host cholesterol. https://www.pnas.org/doi/10.1073/pnas.0711159105 doi:10.1073/pnas.0711159105.
29. Talwar, S. *et al.* Role of VapBC12 Toxin-Antitoxin Locus in Cholesterol-Induced Mycobacterial Persistence. *mSystems* **5**, e00855-20 (2020).
30. Tyagi, S. *et al.* VapC12 ribonuclease toxin modulates host immune response during Mycobacterium tuberculosis infection. *Front. Immunol.* **15**, (2024).
31. Hendon-Dunn, C. L. *et al.* Regrowth of Mycobacterium tuberculosis Populations Exposed to Antibiotic Combinations Is Due to the Presence of Isoniazid and Not Bacterial Growth Rate. *Antimicrob. Agents Chemother.* **63**, e00570-19 (2019).

32. Grzelak, E. M. *et al.* Strategies in anti-Mycobacterium tuberculosis drug discovery based on phenotypic screening. *J. Antibiot. (Tokyo)* **72**, 719–728 (2019).
33. Gill, W. P. *et al.* A replication clock for Mycobacterium tuberculosis. *Nat. Med.* **15**, 211–214 (2009).
34. Krissinel, E. & Henrick, K. Inference of Macromolecular Assemblies from Crystalline State. *J. Mol. Biol.* **372**, 774–797 (2007).
35. Raumann, B. E., Rould, M. A., Pabo, C. O. & Sauer, R. T. DNA recognition by β-sheets in the Arc represser–operator crystal structure. *Nature* **367**, 754–757 (1994).
36. Somers, W. S. & Phillips, S. E. V. Crystal structure of the met represser–operator complex at 2.8 Å resolution reveals DNA recognition by β-strands. *Nature* **359**, 387–393 (1992).
37. Gomis-Rüth, F. X. *et al.* The structure of plasmid-encoded transcriptional repressor CopG unliganded and bound to its operator. *EMBO J.* **17**, 7404–7415 (1998).
38. Singh, A., Mai, D., Kumar, A. & Steyn, A. J. C. Dissecting virulence pathways of Mycobacterium tuberculosis through protein–protein association. *Proc. Natl. Acad. Sci.* **103**, 11346–11351 (2006).
39. Furin, J., Cox, H. & Pai, M. Tuberculosis. *The Lancet* **393**, 1642–1656 (2019).
40. CDCTB. Tuberculosis (TB) - Treatment Regimens for Latent TB Infection. *Centers for Disease Control and Prevention* https://www.cdc.gov/tb/topic/treatment/ltbi.htm (2022).

41. Dutta, N. K. *et al.* Inhibiting the stringent response blocks Mycobacterium tuberculosis entry into quiescence and reduces persistence. *Sci. Adv.* **5**, eaav2104 (2019).
42. Bryk, R. *et al.* Selective killing of nonreplicating mycobacteria. *Cell Host Microbe* **3**, 137–145 (2008).
43. Bryk, R. *et al.* Triazaspirodimethoxybenzoyls as selective inhibitors of mycobacterial lipoamide dehydrogenase. *Biochemistry* **49**, 1616–1627 (2010).
44. Mukherjee, D., Zou, H., Liu, S., Beuerman, R. & Dick, T. Membrane-Targeting AM-0016 Kills Mycobacterial Persisters and Shows Low Propensity for Resistance Development. *Future Microbiol.* **11**, 643–650 (2016).
45. Zhang, Y., Colabroy, K. L., Begley, T. P. & Ealick, S. E. Structural studies on 3-hydroxyanthranilate-3,4-dioxygenase: the catalytic mechanism of a complex oxidation involved in NAD biosynthesis. *Biochemistry* **44**, 7632–7643 (2005).
46. Yam, K. C. *et al.* Studies of a ring-cleaving dioxygenase illuminate the role of cholesterol metabolism in the pathogenesis of Mycobacterium tuberculosis. *PLoS Pathog.* **5**, e1000344 (2009).
47. Abuhammad, A. Cholesterol metabolism: a potential therapeutic target in Mycobacteria. *Br. J. Pharmacol.* **174**, 2194 (2017).
48. Ribeiro-Guimarães, M. L. & Pessolani, M. C. V. Comparative genomics of mycobacterial proteases. *Microb. Pathog.* **43**, 173–178 (2007).
49. Pearce, M. J., Mintseris, J., Ferreyra, J., Gygi, S. P. & Darwin, K. H. Ubiquitin-like protein involved in the proteasome pathway of Mycobacterium tuberculosis. *Science* **322**, 1104–1107 (2008).
50. Hansen, S. *et al.* Regulation of the Escherichia coli HipBA toxin-antitoxin system by proteolysis. *PloS One* **7**, e39185 (2012).

51. Crystal structure of proteolyzed VapBC and DNA-bound VapBC from Salmonella enterica Typhimurium LT2 and VapC as a putative Ca2+-dependent ribonuclease. doi:10.1096/fj.201901989R.
52. Dienemann, C., Bøggild, A., Winther, K. S., Gerdes, K. & Brodersen, D. E. Crystal Structure of the VapBC Toxin–Antitoxin Complex from *Shigella flexneri* Reveals a Hetero-Octameric DNA-Binding Assembly. *J. Mol. Biol.* **414**, 713–722 (2011).
53. Cholesterol Recognition Motifs (CRAC) in the S Protein of Coronavirus: A Possible Target for Antiviral Therapy? | IntechOpen. https://www.intechopen.com/chapters/75030.
54. Fantini, J. & Barrantes, F. J. How cholesterol interacts with membrane proteins: an exploration of cholesterol-binding sites including CRAC, CARC, and tilted domains. *Front. Physiol.* **4**, 31 (2013).
55. Miller, C. M., Brown, A. C. & Mittal, J. Disorder in Cholesterol-Binding Functionality of CRAC Peptides: A Molecular Dynamics Study. *J. Phys. Chem. B* **118**, 13169–13174 (2014).
56. Kabsch, W. XDS. *Acta Crystallogr. D Biol. Crystallogr.* **66**, 125–132 (2010).
57. Evans, P. R. & Murshudov, G. N. How good are my data and what is the resolution? *Acta Crystallogr. D Biol. Crystallogr.* **69**, 1204–1214 (2013).
58. Vonrhein, C. *et al.* Data processing and analysis with the autoPROC toolbox. *Acta Crystallogr. D Biol. Crystallogr.* **67**, 293–302 (2011).
59. Sheldrick, G. M. Experimental phasing with SHELXC/D/E: combining chain tracing with density modification. *Acta Crystallogr. D Biol. Crystallogr.* **66**, 479–485 (2010).

60. Adams, P. D. *et al.* PHENIX: a comprehensive Python-based system for macromolecular structure solution. *Acta Crystallogr. D Biol. Crystallogr.* **66**, 213–221 (2010).
61. Murshudov, G. N. *et al.* REFMAC5 for the refinement of macromolecular crystal structures. *Acta Crystallogr. D Biol. Crystallogr.* **67**, 355–367 (2011).
62. Winn, M. D. *et al.* Overview of the CCP4 suite and current developments. *Acta Crystallogr. D Biol. Crystallogr.* **67**, 235–242 (2011).
63. Painter, J. & Merritt, E. A. Optimal description of a protein structure in terms of multiple groups undergoing TLS motion. *Acta Crystallogr. D Biol. Crystallogr.* **62**, 439–450 (2006).
64. Singh, M., Srivastava, M., Wakode, S. R. & Asthana, S. Elucidation of Structural Determinants Delineates the Residues Playing Key Roles in Differential Dynamics and Selective Inhibition of Sirt1-3. *J. Chem. Inf. Model.* **61**, 1105–1124 (2021).
65. Srivastava, M., Mittal, L., Kumari, A. & Asthana, S. Molecular Dynamics Simulations Reveal the Interaction Fingerprint of Remdesivir Triphosphate Pivotal in Allosteric Regulation of SARS-CoV-2 RdRp. *Front. Mol. Biosci.* **8**, 639614 (2021).
66. Mittal, L., Tonk, R. K., Awasthi, A. & Asthana, S. Targeting cryptic-orthosteric site of PD-L1 for inhibitor identification using structure-guided approach. *Arch. Biochem. Biophys.* **713**, 109059 (2021).
67. Kumari, A., Mittal, L., Srivastava, M., Pathak, D. P. & Asthana, S. Conformational Characterization of the Co-Activator Binding Site Revealed the Mechanism to Achieve the Bioactive State of FXR. *Front. Mol. Biosci.* **8**, 658312 (2021).

68. Purushotham, N. *et al.* Design and synthesis of amino acid derivatives of substituted benzimidazoles and pyrazoles as Sirt1 inhibitors. *RSC Adv.* **12**, 3809–3827 (2022).

Figures and tables

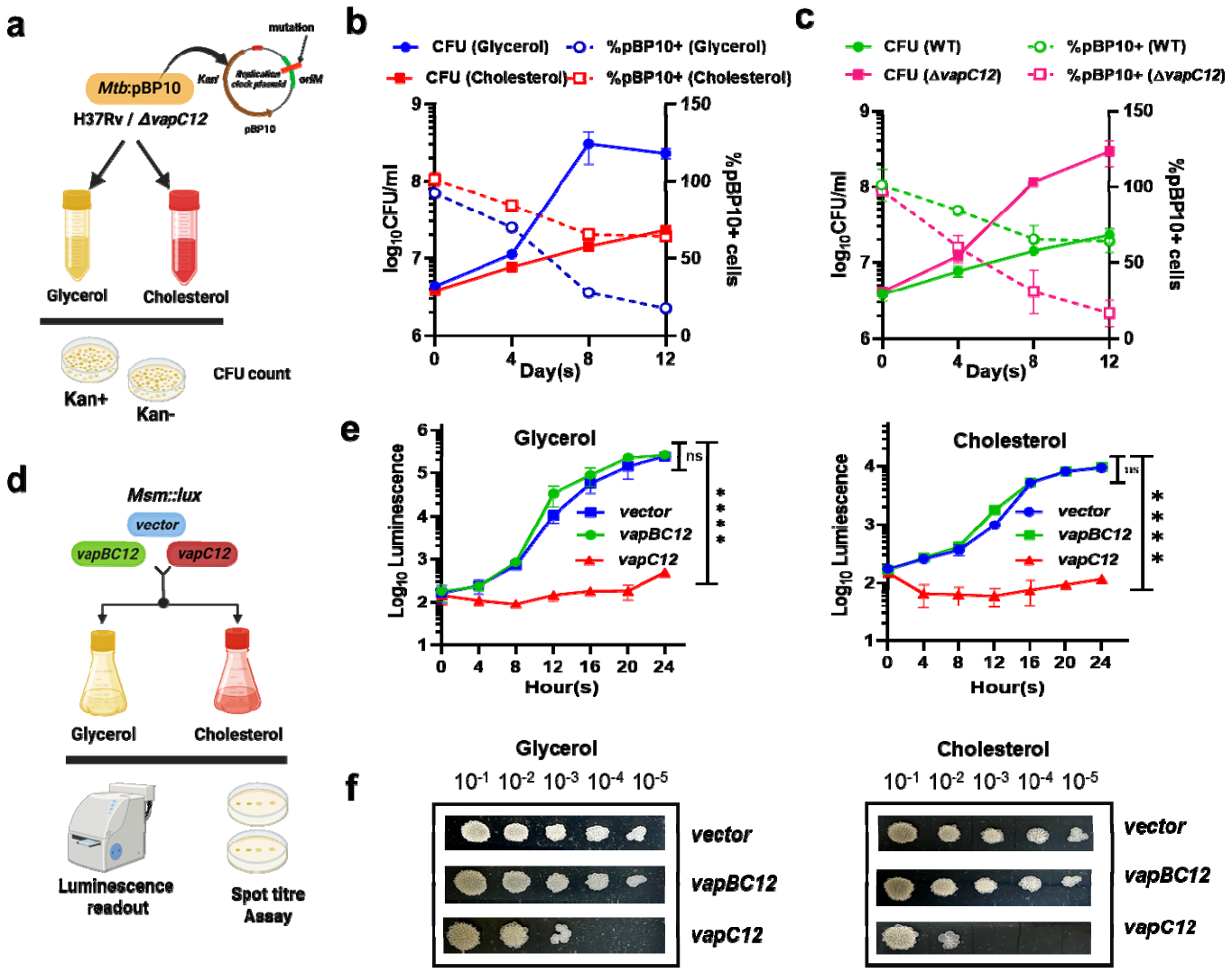

Fig. 1: VapC12 toxin-mediated growth modulation in mycobacteria: a. Diagrammatic representation of the experimental setup to determine replication rates of Rv-WT and VapC12 lacking Mtb using the replication clock plasmid, pBP10, in glycerol and cholesterol media. **b.** Replication of wild-type *M. tuberculosis* in glycerol vs cholesterol media. c. Replication of wild-type *M. tuberculosis* and Δ*vapC12* in cholesterol media as depicted by loss of plasmid with time. **d.** Schematic showing M. smegmatis surrogate model overexpressing *vapBC12* along with luciferase acting as bacterial viability marker. **e.** Growth analysis in *M. smegmatis* model in minimal media supplemented with

glycerol (0.1%) or cholesterol (150µM). Luminescence of the cultures was measured at the indicated time point using SpectraMax iD3 Multi-Mode Microplate Reader. **f.** Spot titre assay after 24 hours of growth in glycerol and cholesterol media, ten-fold serial dilutions of the respective strains were spotted on 7H11 agar plates. The experiments were performed thrice with discrete biological and technical replicates, and the data plotted represent the mean ± SD. Data were analyzed using Tukey's multiple comparisons test (two-way ANOVA) ns, non-significance, ****, P<0.0001.

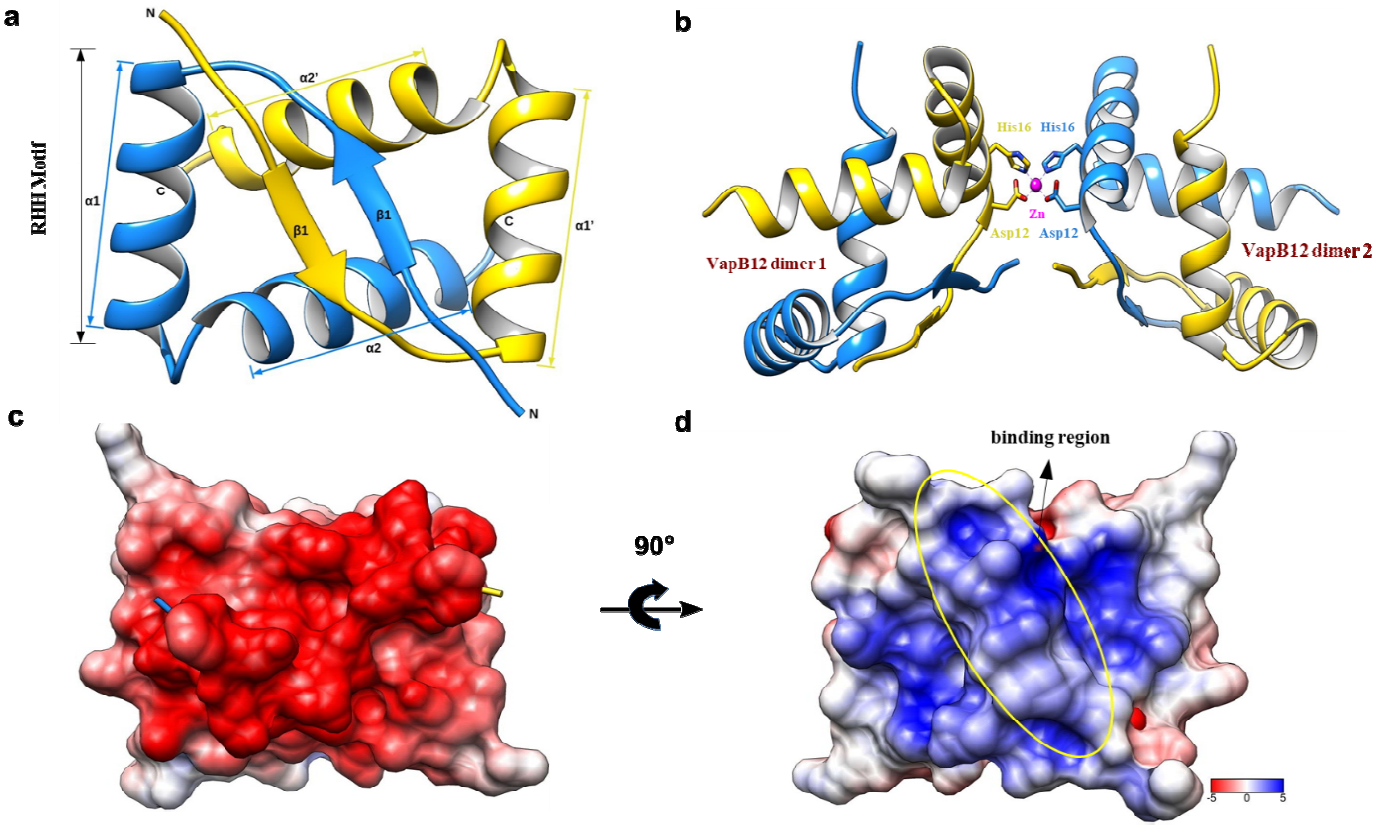

Fig. 2: 1.6 A^0 crystal structure of the homodimeric VapB12 antitoxin. **a.** Monomers of the VapB12 antitoxin are rendered in yellow and blue. The N-terminal DNA-binding ribbon-helix DNA-binding motif (RHH) is labeled. The secondary structural elements (β1, α1, and α2) of VapB12 are labeled on both monomers. **b.** A cartoon representation of two VapB12 dimers stabilized by Zn coordinated by histidine and aspartic residues. **c.** The electrostatic surface of the VapB12 homodimer, calculated using APBS and plotted by Chimera. **d.** View of the VapB12 homodimer with 90° rotation along the x-axis in Fig.2c.

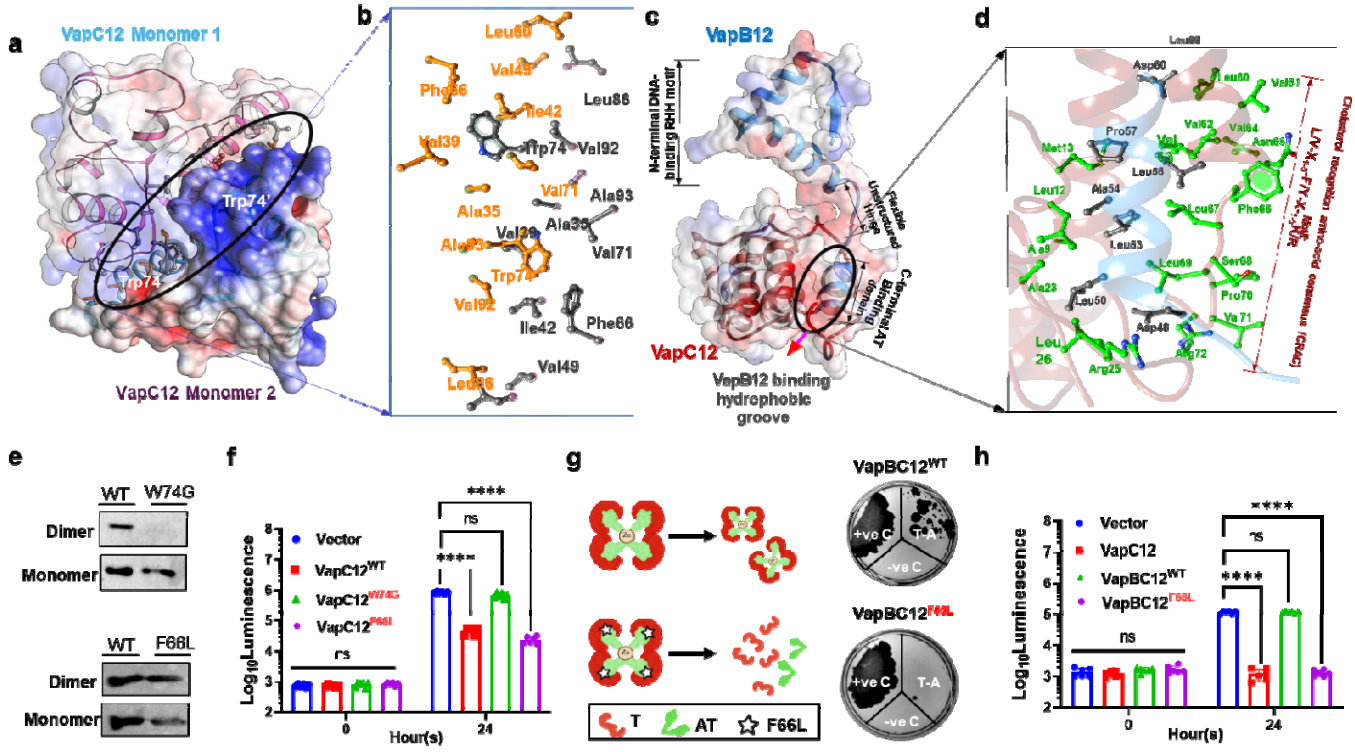

Fig. 3: VapC12 is active in homo-dimeric form and interacts with anti-toxin VapB12 via unique CRAC motif: a-b: Detailed structures of the VapC12 homodimer homology model interface. **a.** The homodimeric interface of VapC12 is indicated by a ribbon representation, and the other part is expressed by a semitransparent electrostatic surface representation. Trp74 has been shown to interact strongly within a hydrophobic pocket formed by residues of another subunit. **b.** Details of the hydrophobic interaction of the VapC12 homodimer interface. Interacting residues belonging to different monomers of VapC12 are colored gray and orange, respectively. c-d**:** Detailed structures of the VapBC12 toxin-antitoxin heterodimeric homology model interface. **c.** The heterodimeric interface of VapBC12 is indicated by a ribbon representation, and a semi-transparent electrostatic surface representation expresses the other part. The black lines indicate different domains of VapC12. **d.** Details of the ionic and hydrophobic interaction of the VapBC12 heterodimer interface. Interacting residues belonging to VapB12 and VapC12 are colored in gray and green, respectively. Residues forming the CRAC motif ([L/I/V]-X1–5-[F]-X1–5-[K/R]) demarcate the antitoxin binding groove in

VapC12, indicated by the maroon arrow. **e.** Western blot for VapC12 protein homodimer and monomer. His-tagged VapC12 protein was heterologously expressed in *E.coli* BL21 DE3. Protein lysate of *E.coli* was incubated with 0.001% glutaraldehyde (GLA) to link the dimeric proteins, and VapC12 protein was detected by developing a western blot using anti-His antibody. The effect of different mutations, one from the hydrophobic core (W74G, top), and the other from the CRAC motif (F66L, bottom), was checked on homo-dimerization of the protein. **f.** Effect of mutations in VapC12 on bacterial growth using *M. smegmatis* model expressing vector alone, $VapC12^{WT}$, $VapC12^{W74G}$ and $VapC12^{F66L}$. **g.** Schematic representation of hetero-octameric $VapBC12^{WT}$ structure (top) and mutated version ($VapBC12^{F66L}$, bottom), positions of the mutation are indicated by stars, and the effect of the mutation is depicted after the black arrow, followed by MPFC-based protein-protein interaction (PPI). **h.** Effect of expression of VapC12, $VapBC12^{WT}$ and $VapBC12^{F66L}$ in of *M. smegmatis* model expressing luciferase as the indicator of bacterial viability. Luminescence of the cultures was measured at the indicated time point using SpectraMax iD3 Multi-Mode Microplate Reader. The experiments (f and h) were performed thrice with discrete biological and technical replicates, and the data plotted represent the mean ± SD. Data were analyzed using a Two-way ANOVA where ns, non-significance; **, $p < 0.01$.

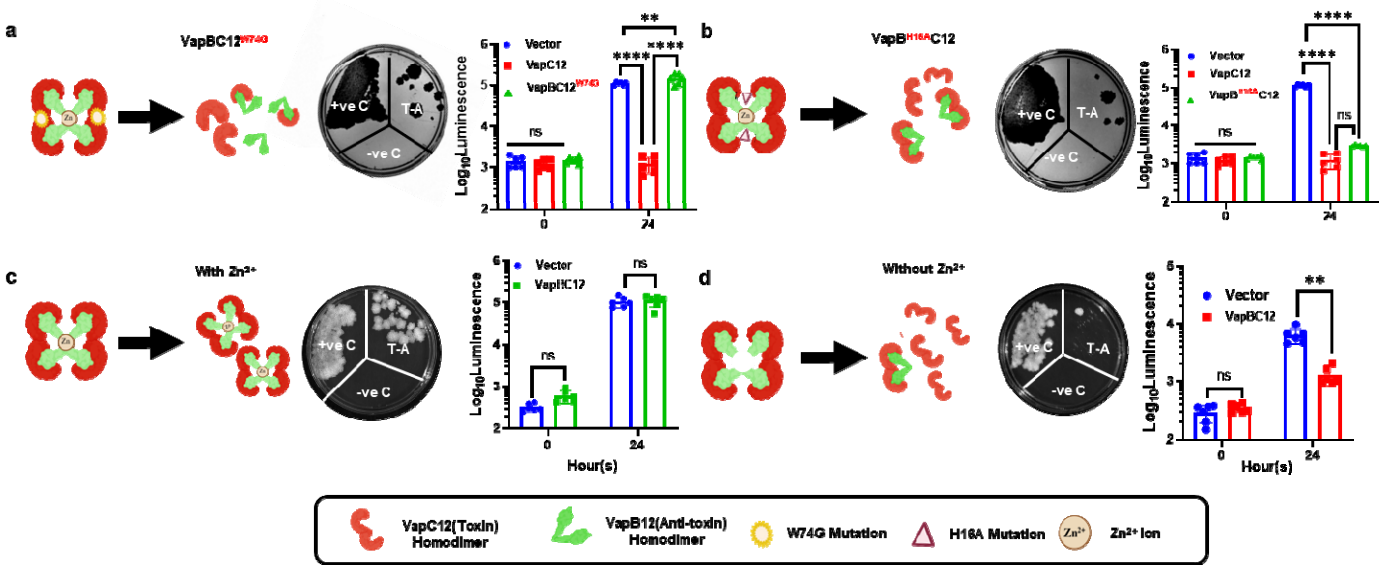

Fig. 4: Functional validation of residues critical for TA interaction: a. Diagrammatic representation of the interaction between VapB12 and VapC12^{W74G}, visualized by MPFC-based PPI interaction. The circle denotes the position of mutation, and the resulting TA complex post-mutation is depicted following an arrow. The PPI result was validated by a growth analysis in *M. smegmatis* strain expressing vector alone, VapC12, VapBC12^{WT}, or VapBC12^{W74G}, depicted in the adjacent bar graph. **b.** Diagrammatic representation of the interaction between VapB^{H16A}12 and VapC12, followed by PPI and *M. smegmatis* growth analysis. **c-d.** The above data were validated by performing PPI and growth analysis of VapBC12^{WT} with and without Zn^{2+} ion. Agar plates were prepared in minimal media supplemented with (c) or without (d) zinc sulphate in addition to trimethoprim 50µg/ml and growth kinetics were performed in glycerol media supplemented with (c) or without (d) zinc sulphate. All strains had constitutively expressed luciferase as the bacterial growth indicator. The Luminescence of the cultures was measured at the indicated time point using the SpectraMax iD3 Multi-Mode Microplate Reader. The experiment was performed in triplicate, and the data plotted represent the mean ± SD, analyzed using Tukey's multiple comparisons test (2-way ANOVA). ns, non-significance; **, $p < 0.01$; ****, $p < 0.0001$.

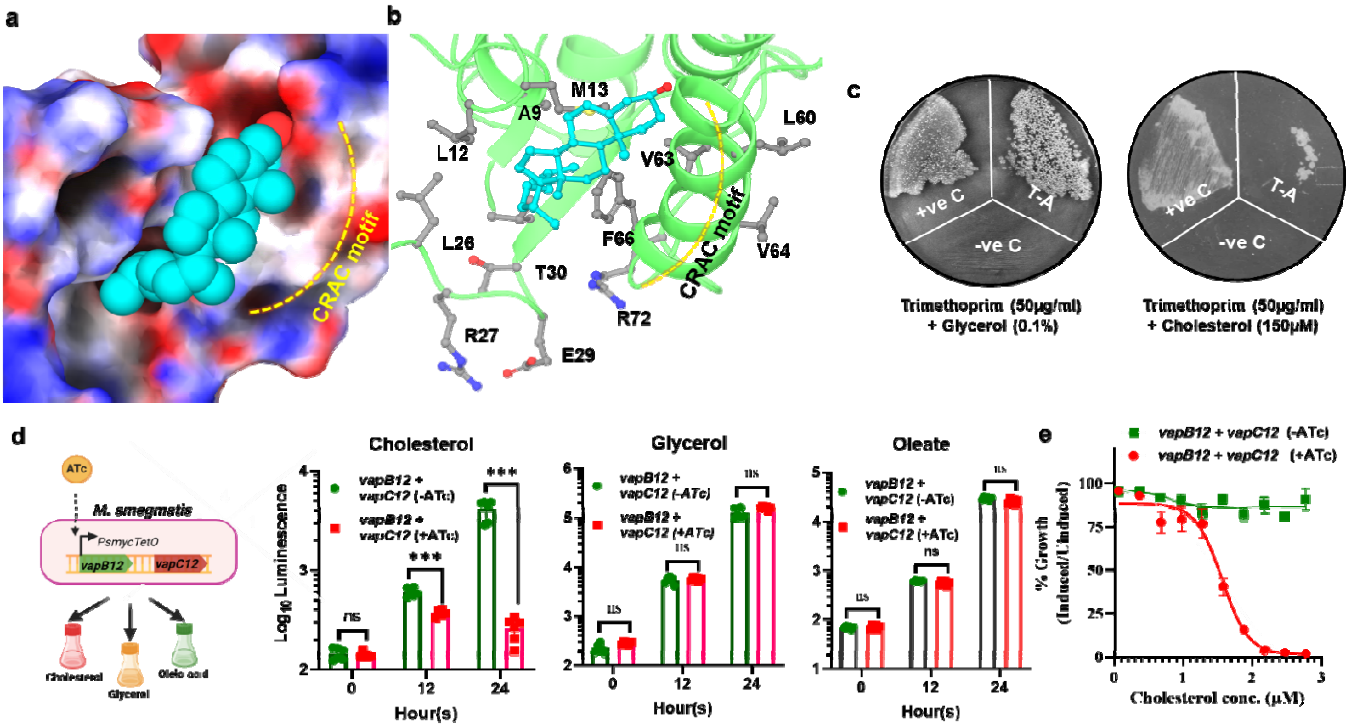

Fig. 5: Competitive displacement of VapB12 antitoxin by cholesterol activates VapC12 toxin: a. Molecular docking of the most populated pose of cholesterol **b.** Binding site residues of toxin, including the CRAC motif. **c.** PPI using MPFC. The transformants of Vector only (-ve C), ESAT-6 & CFP10 (+ve C), and VapC12 & VapB12 (T-A), were cultured in minimal media containing glycerol (0.1%) and cholesterol (150 µM) for 24 hours and streaked onto 7H11 medium containing Trimethoprim (50µg/ml) plus glycerol (0.1%) or cholesterol (150 µM). Growth is indicative of protein–protein interaction. **d.** Growth curves of *M. smegmatis* strains expressing *vapB12* and *vapC12* from the tet-inducible promoter. The log phase culture of the strains was used to set an initial inoculum of 10^5 cells/ml in cholesterol (150µM), glycerol (0.1%), and *oleate* (40 µM) media. Anhydrotetracycline (ATc) was used at a 200 ng/ml concentration. **e.** Dose-response analysis of cholesterol-toxin interaction in *M. smegmatis* model with increasing concentration of cholesterol (µM) in the media. Luminescence, as a measure of bacterial viability was measured at the indicated time point using SpectraMax iD3 Multi-Mode Microplate Readers. The experiment was performed in triplicate, and the data plotted represent

the mean ± SD. The Data were analysed by a two-way ANOVA. ns, non-significance, **, p < 0.01, ***, p <0.001, ****, P<0.0001.

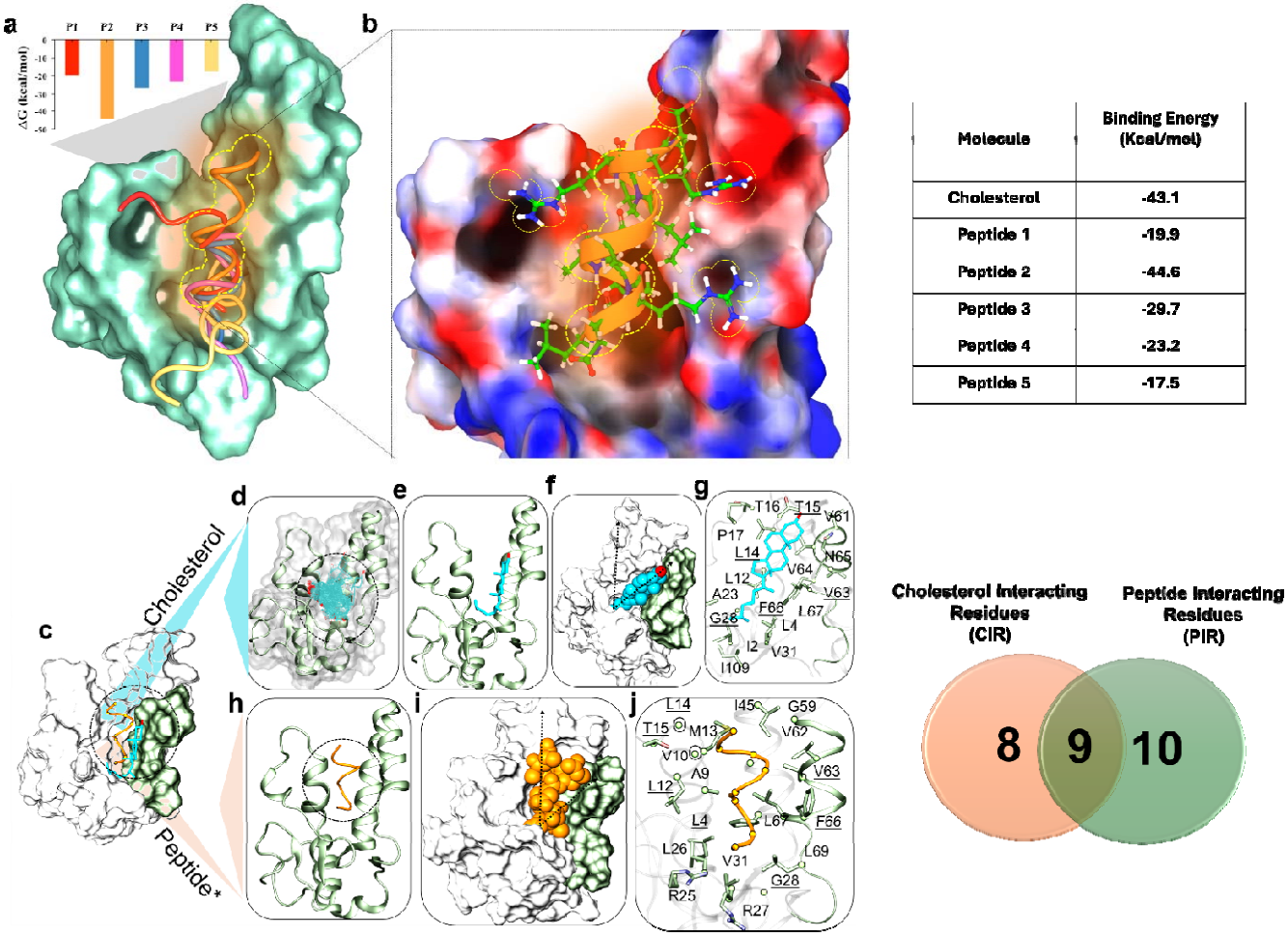

Molecule	Binding Energy (Kcal/mol)
Cholesterol	-43.1
Peptide 1	-19.9
Peptide 2	-44.6
Peptide 3	-29.7
Peptide 4	-23.2
Peptide 5	-17.5

Fig. 6: Generation and selection of Antitoxin mimicking peptides: a. Binding zone and binding free energy of identified peptides (P1 to P5). Exact values of binding energy (kcal/mol) is given in the table alongside **b.** Structural characterization of P2 (the most potent computational hit). The zoom-out view of best best-performing peptide in the form of an electrostatic surface shows the electrostatic complementarity at basic anti-toxin arginine residues (shown by yellow dotted lines) over the acidic toxin surface. **(c-j).** Molecular Interaction fingerprinting (c) Superimposed image of toxin in complex with cholesterol and peptide P2, where protein excluding CRAC motif region of VapC12 is rendered in Surface view and coloured in white, while the CRAC motif region is rendered in Lime. The

cholesterol is rendered in Licorice, Cyan and the peptide* is in Orange and rendered in tube, (d) Focused docking of cholesterol and conformers are shown in Lines: Cyan, (e) Best conformer obtained after FD, (f) molecular dynamics (MD) simulation's energy minimized stable state of cholesterol reveals tight packing and interaction with CRAC motif residues where protein** rendering is as same as in panel (c) and cholesterol is rendered in van der walls (VdW), (g) residues lining cholesterol within 3.5 Å are shown. The residues are rendered in Licorice: Lime and Cα atoms are rendered in CPK: Lime and whole protein** is rendered in transparent new cartoon while the CRAC motif region is in Lime. (h) P2 (peptide*) conformation involved in interaction with CRAC motif residues, (i) Energy minimized stable state of peptide* where protein** rendering is as same as (C) and peptide* rendering is same as cholesterol, (h) residues lining peptide* under 3.5 Å are depicted, rendered as in (g). The residues V10 and L14, in which the sidechain was missing in crystal remain the same here. The common residues are underlined in panels g and h. The change of binding axis between cholesterol and peptide is shown by dotted arrows in panel (f) and (i). Numbers of common interacting residues and those exclusive to cholesterol and peptide is shown in the Venn diagram.

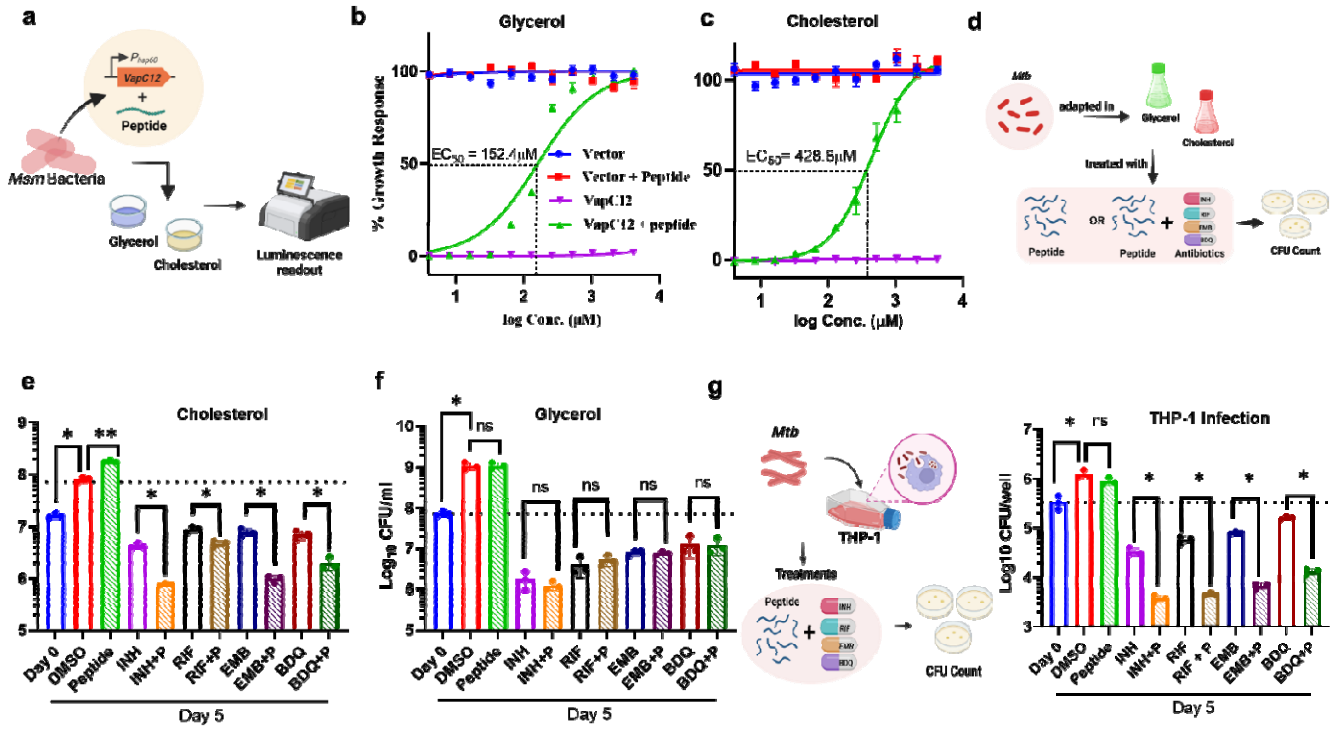

Fig.7: **Anti-toxin mimicking peptide P2 enhances *M. tuberculosis* killing by first and second-line anti-TB drugs: a.** Schematic representation of the assay used to determine potential of anti-toxin peptide in neutralising effects of toxin. P2 peptide dose-response curve (DRC) against toxin activity: strain expressing *vapC12* gene was incubated at density of 10^5 cells/ml in a 96-well white plate with and without P2 peptide in glycerol (0.1%) and cholesterol (150µM) Media. **b-c.** Vector alone was maintained as control. The peptide was two-fold serially diluted to obtain minimum effective concentration (MEC). The black dashed line marks the EC50 (152.4 µM) in glycerol media (c) and (428.8 µM) cholesterol media (d). All strains had constitutively expressed luciferase enzyme and substrates. Luminescence of the cultures was measured at the indicated time point using SpectraMax iD3 Multi-Mode Microplate Readers. **d.** schematic illustration of protocols used in (e-f). *M. tuberculosis* was adapted in glycerol and cholesterol media, when the OD reached 0.2, cultures were treated with antibiotics alone or in combination with 38 µM. CFU was measured to assess the effectiveness of antibiotics. **e-f.** Bar graph representing antibiotic killing test of H37Rv in the presence of 10X MIC of isoniazid (INH), rifampicin (RIF), ethambutol (EMB), bedaquillin (BDQ) alone or in

combination with 38 µM P2 peptide in cholesterol (e) and glycerol (f) media. **g.** Intra-macrophage survival assay using THP-1 monocytes derived macrophages, determined by CFU enumeration. Infection was given at MOI 1:1, and 1X MIC of antibiotics was used to treat infected macrophages. The data plotted represents three biological replicates in mean ± the SD. Data were analyzed using a Two-way ANOVA.

ns, non-significance, **, $p < 0.01$, ***, $p < 0.001$, ****, $P < 0.0001$.

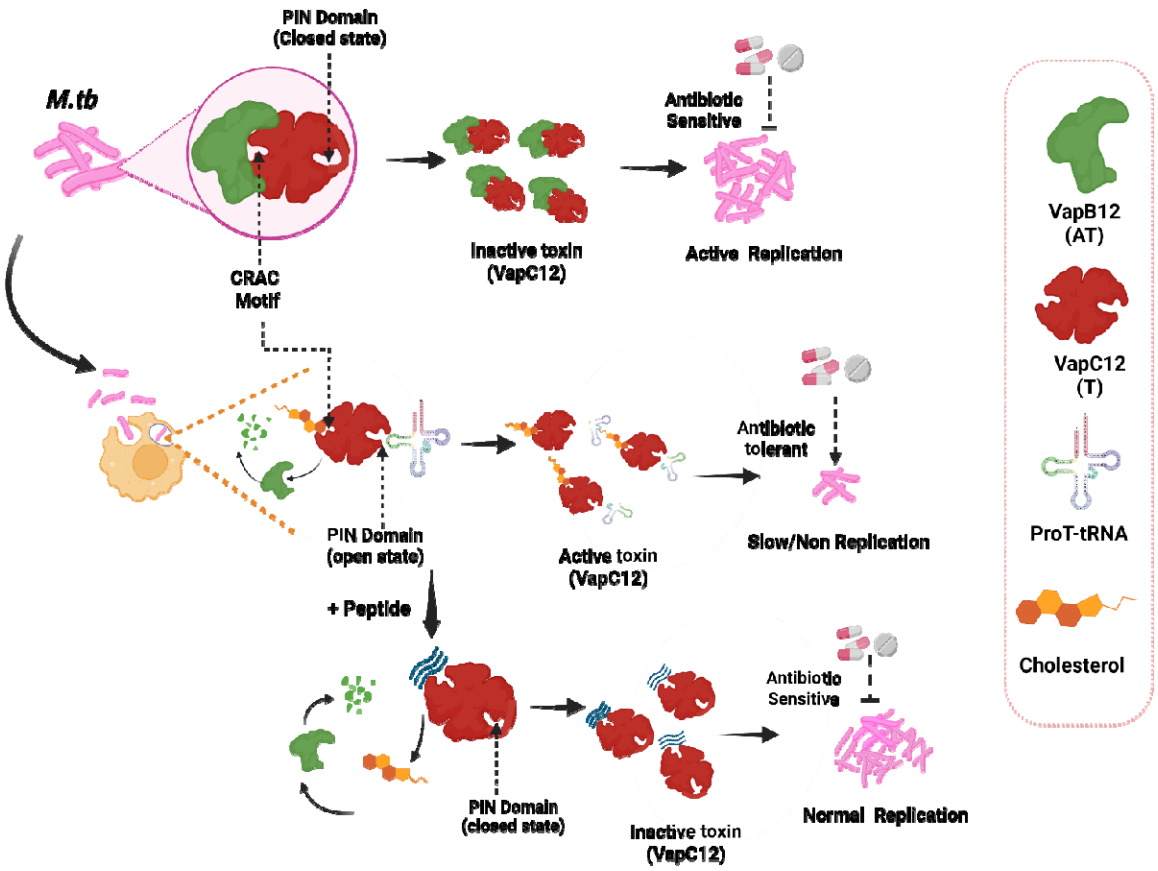

Fig. 8: Graphical summary describing cholesterol-dependent regulation of the VapC12 ribonuclease activity modulating growth and antibiotic tolerance in *M. tuberculosis*. The growth of *M. tuberculosis* is regulated by the VapBC TA system. Under normal growth condition, the VapB12 antitoxin binds to the allosteric site (CRAC motif) of the ribonuclease toxin, locking the catalytic site in a “closed” conformation to ensure continuous bacterial replication. However, during infection, the host cholesterol infiltrates the pathogen and competitively displaces the antitoxin from the CRAC motif of the toxin. The activated VapC12 ribonuclease toxin then retards growth and favors the generation of an antibiotic-tolerant persister population. The synthetic peptide P2, which mimics antitoxin, functions by out-competing the binding ability of the cholesterol to the CRAC motif, keeps the toxin in a constitutively inactive state. Hence, addition of the P2 peptide, that impedes the

ability of *M. tuberculosis* to modulate growth, potentiates the antibacterial activity of the first line anti-TB drugs.

Table 1. Data collection and refinement statistics of VapB12 crystallization

	$LrpA_T$
	Orthorhombic form
Data collection	
Space group	$P\ 4_1$
Cell dimensions	
a, *b*, *c* (Å)	34.66, 34.66, 162.23
a, *b*, *g* (°)	90, 90, 90
X-ray source	ID23-1, ESRF
Wavelength (Å)	0.979507
Resolution range (Å)	40.55-1.64 (1.66-1.64)
No. of unique reflections	23505 (1174)
R_{merge}	0.06 (0.79)
R_{pim}	0.02 (0.34)
$I/s(I)$	12.6 (2.0)
$CC_{1/2}$	0.99 (0.81)
Completeness (%)	99.9 (99.7)
Multiplicity	7.0 (6.3)
Refinement	
R_{work} / R_{free}	0.172/0.218
Nonhydrogen atoms	1481
Mean *B* factors (Å^2)	38.85
R.m.s. deviations	
Bond lengths (Å)	0.011
Bond angles (°)	1.568

Ramachandra plot -favored/allowed/outliers (%)	100/0/0
PDB ID	7E4J